Hybrid Microwave Imaging of 3-D Objects Using LSM and BIM Aided by a CNN U-Net

Feng Han, *Senior Member, IEEE*, Miao Zhong, and Junjie Fei

***Abstract*— This article presents an efficient and accurate 3-D quantitative hybrid microwave imaging (MWI) method. The linear sampling method (LSM) is first carried out to quickly find the approximate shapes and locations of the unknown objects in the imaging domain based on the scattered field data recorded by receivers which are placed in the far-field zone and wrap the domain. Then the full-wave inversion (FWI) is implemented in a downsized domain which tightly encloses the unknown objects instead of in the whole domain through the Born iterative method (BIM) to quantitatively retrieve the dielectric model parameters of the objects. Because the LSM fails to obtain the sufficiently accurate shapes of the unknown objects, a trained 3-D convolutional neural network (CNN) U-Net is inserted between the LSM imager and the BIM solver to further refine the obtained shapes of LSM, which is expected to aid the following FWI. The proposed hybrid method is validated via the quantitative imaging of both inhomogeneous isotropic scatterers and multiple homogeneous anisotropic scatterers. It is shown that the hybrid method can achieve both higher reconstruction accuracy and lower computational cost compared with direct BIM inversion. Meanwhile, its antinoise ability is also tested.**

***Index Terms*— Convolutional neural network (CNN), full-wave inversion (FWI), linear sampling method (LSM), microwave imaging (MWI).**

I. Introduction

MICROWAVE imaging (MWI) is ubiquitous in modern military and civil activities such as radar remote sensing [1], city antiterrorism [2], mine detection [3], security screening [4], diagnosis of breast cancer [5], and inspection of subsurface anomalies [6]. The specific implementation of fast and accurate MWI attracts the tremendous interest of researchers in recent years [7], [8], [9].

Different MWI application scenarios have different requirements for speed and accuracy. In many real-time applications, e.g., through-the-wall imaging for antiterrorism [10], qualitative MWI techniques are always adopted since they can provide instantaneous approximate images of unknown targets. Representative methods include tomography, migration, sampling methods, etc. Tomography utilizes the change of amplitude or phase when a high-frequency microwave passes through the target to obtain its dielectric images [11]. By contrast, diffraction tomography uses the diffraction of low-frequency electromagnetic (EM) waves around the target to reconstruct its parameters by Born approximation (BA) or Rytov approximation (RA). It has been widely employed in geophysical exploration [12]. Migration accomplishes target image focusing through time correlation between the EM pulse signals recorded at the receiver array and the diffusion waves reflected by the target [13]. Sampling methods are actually to convert the EM field recorded at the receiver array into the far-field spherically symmetric wave radiated by a fictitious focal source in the imaging domain. Typical methods include linear sampling method (LSM) [14], direct sampling method (DSM) [15], orthogonality sampling method (OSM) [16], factorization method (FM) [17], etc. Unfortunately, although this qualitative MWI method can obtain the approximate target image in a quite short-time period, the target dielectric parameters, e.g., permittivity and conductivity, are missing.

The quantitative MWI which is frequently realized by full-wave inversion (FWI) is able to overcome this shortcoming by strictly solving the wave equation, e.g., the integral equation. Nevertheless, due to the intrinsic nonlinearity of the EM inverse scattering, the unknown model parameters are usually solved by means of iteratively minimizing an objective function that reflects the mismatch between the measured scattered field data and the forward model-simulated data. Representative iterative methods include the Born iterative method (BIM) [18], contrast source inversion (CSI) [19], subspace optimization method (SOM) [20], and their variants [21], [22] as well as the hybridization [23], [24], etc. The detailed implementation of these iterative methods is quite mature and will not be repeated here. However, although these iterative FWI methods are capable of reconstructing both shapes and dielectric parameters of unknown objects simultaneously, they suffer from unaffordable computational costs. This is especially obvious for the multiparametric 3-D FWI of arbitrary anisotropic scatterers [25].

Therefore, in this article, we extend the 2-D threefold hybrid method presented in our previous work [26] to 3-D scenarios and make use of the respective advantages of the qualitative 3-D LSM imaging technique and the quantitative 3-D BIM FWI. Similar as in [26], the LSM is first used to quickly reconstruct the approximate 3-D shapes of unknown objects in the imaging domain. Then, BIM is implemented in the compressed 3-D regions which tightly wrap the objects. Meanwhile, a 3-D convolutional neural network (CNN) U-Net is used to refine the shapes of the objects obtained by the 3-D LSM. Its usefulness and effectiveness have been validated in [27]. The key innovation point of our work is

Manuscript received 23 June 2022; revised 3 August 2022 and 13 September 2022; accepted 19 September 2022. Date of publication 21 September 2022; date of current version 7 October 2022. *(Corresponding author: Feng Han.)*

The authors are with the Institute of Electromagnetics and Acoustics and the Key Laboratory of Electromagnetic Wave Science and Detection Technology, Xiamen University, Xiamen 361005, China (e-mail: feng.han@xmu.edu.cn).

Digital Object Identifier 10.1109/TGRS.2022.3208450

the threefold hybrid 3-D MWI method. Compared with the pure qualitative MWI method, e.g., LSM, the proposed hybrid method can obtain both the shapes and dielectric information of the unknown objects. Nevertheless, compared with the pure quantitative MWI method, e.g., BIM, the proposed method can accomplish FWI with lower computational cost and achieve higher inversion accuracy due to the downsized computational domain. In addition, it is worth mentioning the difference between this work and [26] and [27]. The research work in [26] is focused on 2-D applications. Therefore, both the formulas of LSM and BIM are mathematically derived in a 2-D framework. Besides, the CNN U-Net in [26] is also 2-D and only 2-D isotropic objects are reconstructed. In [27], although both the 3-D LSM and BIM are adopted, they are for near-field measurement. The transmitters and receivers are placed in a plane just above the subsurface imaging region. In our work, we focus on 3-D MWI applications. The transmitter and receiver arrays wrap the imaging domain and are placed in the far-field zone. This leads to different LSM formulas and also completely different 3-D imaging results which will be shown in Section III. In addition, in this work, the proposed hybrid method is applied to the quantitative MWI of 3-D anisotropic objects, which has never been discussed in [26] and [27]. Finally, we want to emphasize the difference between our work and some other hybrid 3-D MWI methods which also utilize CNN. For example, in [28] and [29], the CNN is used to reconstruct the dielectric images from magnetic resonance or ultrasound images of tissues. In [30], the CNN directly obtains the image of the 3-D volume moisture content from scattered field data. In our work, the CNN U-Net only deals with the shapes of 3-D objects. The dielectric parameters are completely reconstructed by the FWI BIM.

The rest of this article is organized as follows. In Section II, the detailed theory including the 3-D LSM for the far-field measurement and the 3-D BIM for the reconstruction of anisotropic objects is described. In Section III, two numerical cases are presented to validate the proposed hybrid method. The first case is for the reconstruction of 3-D isolated and isotropic inhomogeneous scatterers. The second case is for the inversion of multiple homogeneous anisotropic scatterers and the simulated scattered field data are contaminated by Gaussian noise. Finally, in Section IV, the conclusion is drawn.

II. Methods

In this section, we first briefly describe the mathematical formulas of 3-D LSM used for far-field MWI. Their difference with respect to those of the 3-D LSM used for near-field measurement can be found by comparing the content in Section II-A in this article and that in [27, Sec. II-A]. Then, the full-wave forward and inverse scattering formulas for anisotropic objects are concisely described in the framework of integral equations. Finally, the 3-D CNN U-Net used to refine the LSM images is simply mentioned.

A. 3-D LSM for Far-Field MWI

As shown in Fig. 1, D denotes the 3-D imaging and inversion domain which is discretized into several independent

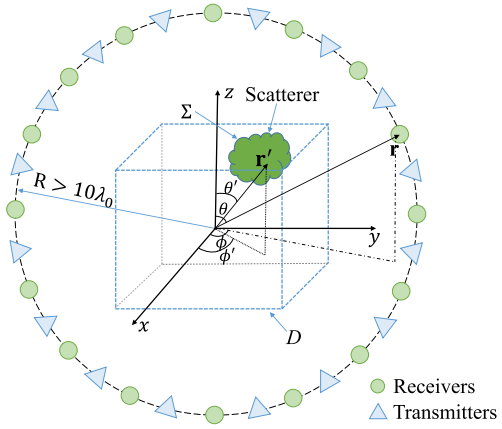

Fig. 1. Three-dimensional MWI and FWI model configuration.

voxels. The location of each voxel is denoted by $\mathbf{r}'$ which represents one spatial sampling point of the 3-D LSM. $\Sigma \subseteq D$ denotes the support of the scatterer. The transmitters and receivers are placed on a spherical surface located in the far zone (i.e., at a distance $R \geq 10\lambda_0$, where λ_0 is the wavelength in the background free space). The 3-D LSM is to determine the gain matching relationship between the scattered field data recorded at the far-field receiver array and the 3-D Green's function corresponding to the fictitious source point located at $\mathbf{r}'$. The obtained gain is expected to be limited if $\mathbf{r}' \in \Sigma$ but infinitely large if $\mathbf{r}' \notin \Sigma$ [31].

Suppose there are totally N_t transmitters and N_r receivers placed on the far-field spherical surface with the radius R. Because the 3-D LSM requires multiview and multistatic EM data with multipolarization [31], we invoke the $\hat{\theta}$ and $\hat{\phi}$ components of the electric fields in the LSM formulas. For the incident electric field E^{θ}_{inc} or E^{ϕ}_{inc} and the recorded scattered electric field E^{θ}_{sct} or E^{ϕ}_{sct}, we can assemble four $(N_r \times N_t)$-dimensional multistatic scattered field data matrix $\mathbf{F}^{p,q}$ where p and q can either be θ or ϕ. The generic element of $\mathbf{F}^{p,q}$ is the $\hat{q}$ polarized scattered electric field measured at the mth receiver when the nth transmitter emits a $\hat{p}$ polarized electric field [31]. Assuming that the solution of 3-D LSM is the $(2N_t)$-dimensional unknown vector $\mathbf{g}_u = [\mathbf{g}^{\theta}_u(\mathbf{r}'), \mathbf{g}^{\phi}_u(\mathbf{r}')]$, then the formula of LSM can be written as follows:

$$\mathbf{F}\mathbf{g}_u = \begin{bmatrix} \mathbf{F}^{\theta,\theta} & \mathbf{F}^{\theta,\phi} \\ \mathbf{F}^{\phi,\theta} & \mathbf{F}^{\phi,\phi} \end{bmatrix} \begin{bmatrix} \mathbf{g}^{\theta}_u(\mathbf{r}') \\ \mathbf{g}^{\phi}_u(\mathbf{r}') \end{bmatrix} = \begin{bmatrix} \mathbf{f}^{\theta}_u(\mathbf{r}', \mathbf{r}) \\ \mathbf{f}^{\phi}_u(\mathbf{r}', \mathbf{r}) \end{bmatrix} = \mathbf{f}_u(\mathbf{r}', \mathbf{r}) \quad (1)$$

where $\mathbf{f}^{p}_u(\mathbf{r}', \mathbf{r})$ is the $\hat{p}$ component of the far-field Green's function linking the fictitious source point at $\mathbf{r}'$ in the imaging domain D and the receiver locating at $\mathbf{r}$. The subscript $u = x, y$, or z means the fictitious source can be polarized in $\hat{x}$, $\hat{y}$, or $\hat{z}$ directions, respectively. The evaluation of $\mathbf{f}^{p}_u$ is given in the Appendix. $\mathbf{g}_u$ is the indicator of the support of the 3-D scatterer and its solving process is the same as that given in [27]. The final 3-D LSM image $G(\mathbf{r}')$ is obtained by

$$G(\mathbf{r}') = \log\left(\frac{1}{3}\sum_{u=x,y,z}\frac{1}{\left\|\hat{\mathbf{g}}_u\right\|_2^2}\right) \quad (2)$$

where $\|\|_2$ denotes the L_2 norm. G is expected to be large if $\mathbf{r}'$ locates inside the scatterer but small if it is outside the scatterer. In addition, it has a blurred boundary [31] and

the intact 3-D shape can be obtained via threshold cut. The corresponding mathematical formula has been given by [27, eq. (11)]. One should note that the threshold value used in the cut is obtained by multiplying an empirical constant with the maximum value of G in all the discretized voxels to achieve the best shape [27], [31].

B. 3-D FWI by BIM for Anisotropic Scatterers

As shown in Fig. 1, the scatterer embedded in the inversion domain of free space is assumed to be nonmagnetic and has dielectric arbitrary anisotropy. Its complex relative permittivity tensor is computed by

$$\overline{\overline{\epsilon}} = \begin{bmatrix} \varepsilon_{11} & \varepsilon_{12} & \varepsilon_{13} \\ \varepsilon_{21} & \varepsilon_{22} & \varepsilon_{23} \\ \varepsilon_{31} & \varepsilon_{32} & \varepsilon_{33} \end{bmatrix} + \frac{1}{j\omega\varepsilon_0} \begin{bmatrix} \sigma_{11} & \sigma_{12} & \sigma_{13} \\ \sigma_{21} & \sigma_{22} & \sigma_{23} \\ \sigma_{31} & \sigma_{32} & \sigma_{33} \end{bmatrix} \tag{3}$$

where $\varepsilon_{pq} = \varepsilon_{qp}$ and $\sigma_{pq} = \sigma_{qp}$ with $p, q = 1, 2$ and 3. Note only the symmetrical tensors which are ubiquitous in nature [32] are considered. The forward scattering is described by the electric field integral equation (EFIE) [25]

$$\mathbf{E}_{\text{inc}}(\mathbf{r}) = \mathbf{E}_{\text{tot}}(\mathbf{r}) - \mathbf{E}_{\text{sct}}(\mathbf{r}) = \overline{\overline{\epsilon}}^{-1}(\mathbf{r}) \frac{\mathbf{D}_{\text{tot}}(\mathbf{r})}{\varepsilon_0} - j\omega \int_D \overline{\overline{\mathbf{G}}}_{\mathbf{EJ}}(\mathbf{r}, \mathbf{r}') \cdot \overline{\overline{\chi}}(\mathbf{r}') \mathbf{D}_{\text{tot}}(\mathbf{r}') d\mathbf{r}' \tag{4}$$

where $\overline{\overline{\mathbf{G}}}_{\mathbf{EJ}}$ is the dyadic Green's function (DGF) in the homogeneous free space [33] and $\overline{\overline{\chi}}$ is contrast function which is defined as

$$\overline{\overline{\chi}}(\mathbf{r}) = [\overline{\overline{\epsilon}}(\mathbf{r}) - \overline{\overline{\mathbf{I}}}] \overline{\overline{\epsilon}}^{-1}(\mathbf{r}). \tag{5}$$

In numerical computation, (4) is discretized and $\mathbf{D}_{\text{tot}}$ is expanded by the rooftop basis functions. The coefficients are solved by the stabilized biconjugate-gradient fast Fourier transform (BCGS-FFT). Details can be found in [25] and [34] and will not be repeated here.

The inverse scattering from anisotropic scatterers is formulated by the data equation which is expressed as [25]

$$\mathbf{E}_{\text{sct}}(\mathbf{r}) = j\omega \int_D \overline{\overline{\mathbf{G}}}_{\mathbf{EJ}}(\mathbf{r}, \mathbf{r}') \cdot \overline{\overline{\chi}}(\mathbf{r}') \mathbf{D}_{\text{tot}}(\mathbf{r}') d\mathbf{r}' \tag{6}$$

where $\mathbf{E}_{\text{sct}}$ is the scattered EM field recorded at the receiver array. In the numerical computation, (6) is discretized and the matrix-form equation including the sensitivity matrix which is composed of total field $\mathbf{E}_{\text{tot}}$ and DGFs is obtained [25]. However, because $\mathbf{E}_{\text{tot}}$ also depends on the unknown contrast $\overline{\overline{\chi}}$, the matrix-form equation is nonlinear and can only be solved via iterations. We linearize the equation by replacing $\mathbf{E}_{\text{tot}}$ in the current iterative step with that obtained in the last step by the forward solver BCGS-FFT, and construct the L_2 norm cost function in the framework of BIM [35]

$$\mathbf{C}(\mathbf{x}_k) = \frac{\|\mathbf{b} - \mathbf{A}_{k-1}\mathbf{x}_k\|_2^2}{\|\mathbf{b}\|_2^2} + \gamma \frac{R(\mathbf{x}_k)}{R(\mathbf{x}_{k-1})} \tag{7}$$

in which $\mathbf{b}$ is a column vector including the measured scattered field data, $\mathbf{A}_{k-1}$ is the Fréchet derivative matrix being composed of DGF and $\mathbf{E}_{\text{tot}}$ solved by BCGS-FFT in the $(k-1)$th step, and $\mathbf{x}_k$ is a vector containing the unknown model parameters to be solved in the current iterative step. γ is the regularization factor and R is the total variational (TV) regularization which is written as

$$R(\mathbf{x}) = \left\| \sqrt{(\mathbf{D}_x\mathbf{x})^2 + (\mathbf{D}_y\mathbf{x})^2 + (\mathbf{D}_z\mathbf{x})^2} \right\|_1 \tag{8}$$

where $\|\cdot\|_1$ stands for the L_1 norm and $\mathbf{D}_x$, $\mathbf{D}_y$, and $\mathbf{D}_z$ denote the discrete difference matrices in three directions [36]. Compared with (7) and (8) given in [27], the only difference here is that we consider the dielectric arbitrary anisotropy of the scatterer. Therefore, the vector $\mathbf{x}$ in (7) also contains the nondiagonal elements of dielectric tensors and the sensitivity matrix $\mathbf{A}$ has corresponding additional columns. Finally, it is worth mentioning that the aforementioned mathematical derivations can easily degenerate into isotropic EM scattering ones which will be used in the following Case 1 although their current forms are only derived for anisotropic scatterers.

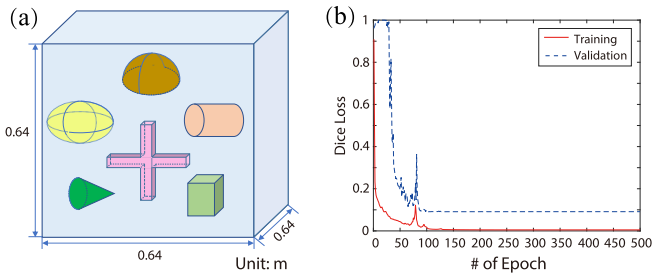

Fig. 2. (a) Isotropic 3-D samples used for training the U-Net. (b) Convergence curves of training and validation.

C. 3-D CNN U-Net

The 3-D CNN U-Net is placed between the LSM imager and the BIM solver. Its purpose is to refine the 3-D image output from the LSM algorithm. The U-Net used in this article is the same as that used in [27] and its details can be found in [27, Sec. II-C]. Its input is the LSM image. Its output is the ground truth shape of the unknown object in the training procedure. The loss function and the training method are also the same as those in [27]. Details will not be repeated here. The training samples and their dielectric parameters are different. They will be displayed in Section III.

III. Numerical Results

In this section, we use two numerical cases to verify the proposed hybrid 3-D MWI method. In the first case, an inhomogeneous scatterer is located in free space. Both the permittivity and conductivity are reconstructed. In the second case, two isolated homogeneous but dielectric arbitrary anisotropic scatterers are reconstructed. The reconstruction ability of multiple anisotropic objects, antinoise ability as well as generalization ability of the proposed MWI method are validated. For the 3-D LSM, the operation frequency is 1 GHz in the first case. However, it is increased to 1.6 GHz in the second case to enhance the imaging resolution. In both cases, the operation frequency is lowered to 300 MHz in the FWI to ensure BIM iteration stability. Transmitters are placed on a sphere surface with a radius of infinite large, i.e., the incident

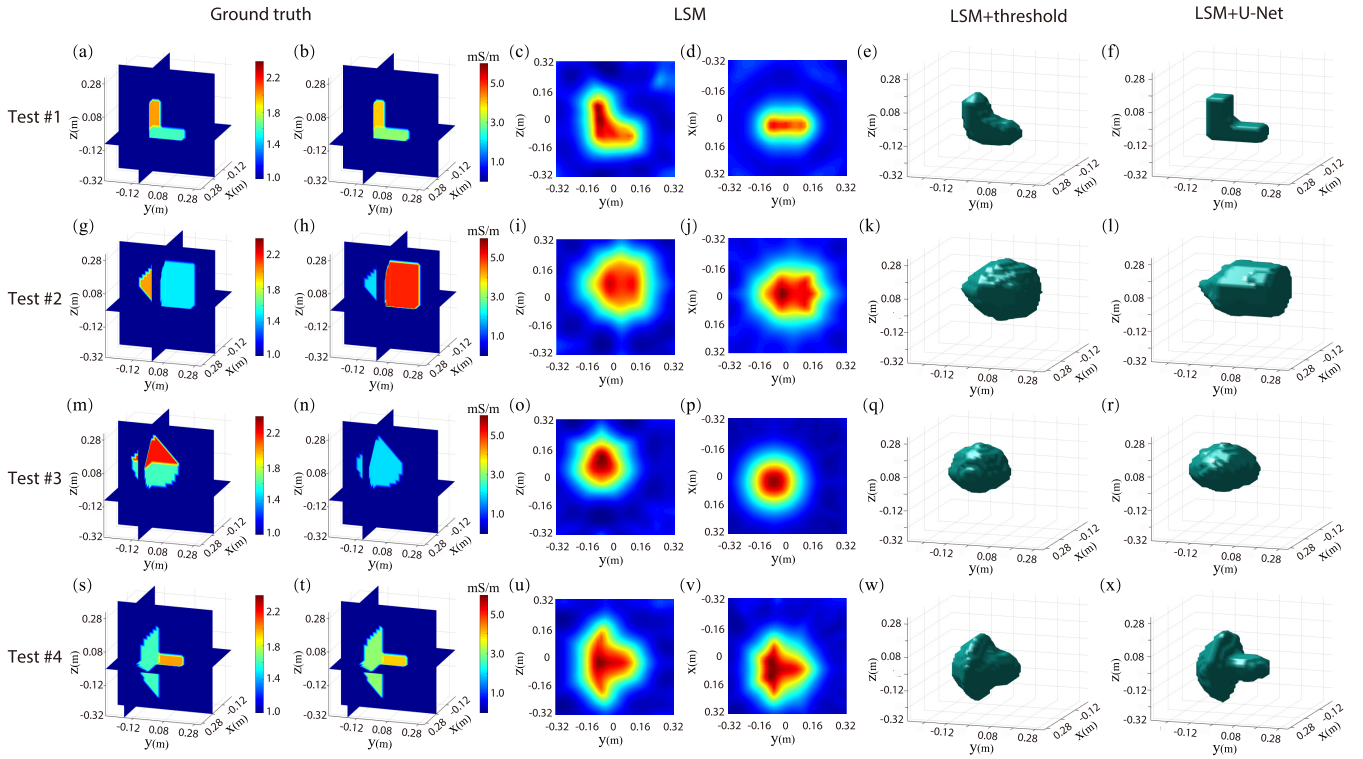

Fig. 3. True 3-D profiles of the inhomogeneous objects, their LSM imaging results, and the voxel classification results in the four tests. Columns 3 and 4 show the 2-D yz and xy LSM imaging slices, respectively. Column 5 shows the LSM results based on the threshold cut. Column 6 shows the LSM results based on 3-D U-Net refinement.

field is a plane wave. Receivers are placed on a sphere surface that has a radius of 10 m. For the 3-D LSM, the transmitter array and the receiver array are arranged in the sphere surface with equal arc-length step. In both $\hat{\theta}$ and $\hat{\phi}$ directions, the angle step is 30°. So, there are totally 84 transmitters. The receiver number is decreased to 62 because all the receivers in the north pole or the south pole corresponding to different ϕ values are overlapped to one receiver. For the 3-D FWI by BIM, the angle step in the $\hat{\phi}$ direction is increased to 60°. Therefore, there are totally 42 transmitters and 32 receivers used for the FWI. For this configuration of transmitters and receivers, numerical simulations show that further increasing their numbers has no aid for the LSM imaging and BIM inversion results while decreasing their numbers will compromise the results. The inversion domain has the dimensions of $0.64 \times 0.64 \times 0.64$ m and is divided into $32 \times 32 \times 32$ voxels. Its center is at the origin. The measured scattered field data used in this article are simulated by the BCGS-FFT forward solver. The model misfit and data misfit defined in [37, eqs. (16) and (17)] are used to indicate the inversion performance. The stopping criterion of iterations of BIM is that the data misfit is less than 0.9% or its relative change in two consecutive iterations is less than 0.4%. All the numerical experiments are performed on a workstation with a 44-core Intel Xeon 6161 2.2 G CPU and 1024 GB RAM.

A. Case 1: An Inhomogeneous Isotropic Object

Similar to [27], we use homogeneous 3-D objects to train the U-Net but use inhomogeneous objects to test its generalization ability. As shown in Fig. 2(a), the training dataset includes six types of simple shapes. They are cones, ellipsoids, cuboids, cylinders, hemispheres, and random combinations of cuboids (forming the cross shape). For each training sample, only one homogeneous object with a random size is placed in a random position of the inversion domain. There are totally 3000 samples used for training and 500 ones for validation. The relative permittivity values of these samples fall between 1.2 and 2.5 while the conductivity values are between 1.0 and 6.0 mS/m. As shown in Fig. 2(b), the final training loss keeps at 0.005 while the validation loss remains at 0.09 after 500 epochs. We then use an inhomogeneous "L" shape, a warehouse, an ice cream, and a mushroom to test the hybrid MWI method. The 3rd and 4th columns in Fig. 3 show the LSM images obtained by (2). We can see that the 2-D slices in both yz and xy planes are close to the true cross sections. This implies that the 3-D images reconstructed by LSM resemble the true 3-D shapes shown in the 1st and 2nd columns. Then, the 5th column of Fig. 3 shows the 3-D shapes obtained by threshold cut while the 6th column shows those obtained by U-Net. Obviously, the U-Net can significantly improve the reconstructed 3-D shapes.

Then, we implement BIM to reconstruct both the permittivity and conductivity of the two inhomogeneous objects in Tests #1–4. The FWI is carried out in the whole inversion domain, in the imaging region judged by threshold cut, and in the imaging region recovered by the 3-D U-Net, respectively. The inverted relative permittivity and conductivity distributions are shown in Figs. 4 and 5. We can see that only a blurry object with small permittivity and conductivity values is obtained if BIM is carried out in the whole inversion domain.

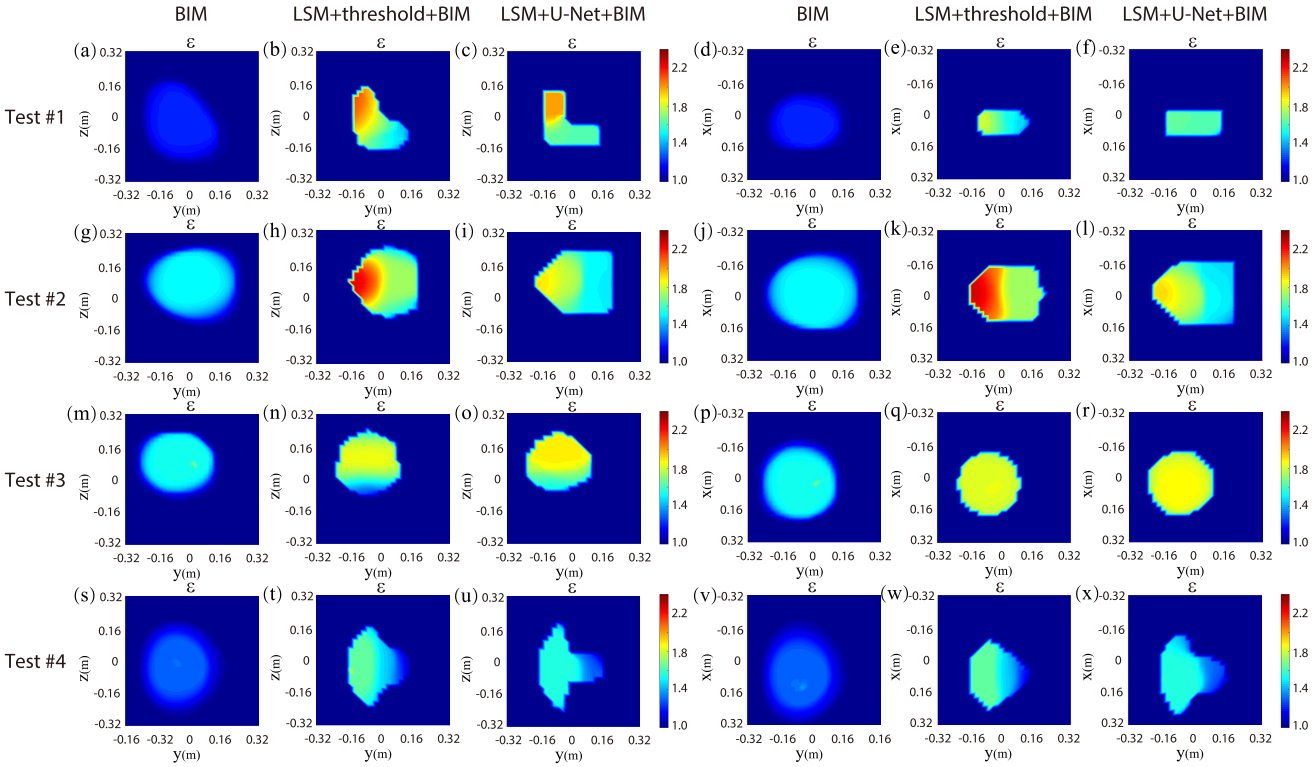

Fig. 4. FWI of relative permittivity values by BIM performed in the whole inversion domain, in the imaging region obtained by threshold cut, and in the imaging region refined by U-Net. Columns 1–3 show the 2-D yz slices of inversion results. Columns 4–6 show the 2-D xy slices of inversion results.

The shapes of the reconstructed objects are not discernible. Then, if we implement BIM in the downsized inversion domain obtained by the threshold cut, the obtained dielectric profiles are significantly improved, as shown in the 2nd and 5th columns of Figs. 4 and 5. However, there are still obvious discrepancies between the reconstructed shapes and dielectric parameter values and their ground truths. These discrepancies are obviously reduced if BIM is implemented in the downsized inversion domain obtained by 3-D U-Net refinement, as shown in the 3rd and 6th columns of Figs. 4 and 5. The 3-D U-Net is capable of generating accurate shapes of the objects from LSM images acquired from far-field measurements, which guarantees the successful applications of the proposed hybrid method to quantitative 3-D MWI.

The data misfit variations in Tests #1–4 are shown in Fig. 6. We can see that the data misfits of Tests #1, #3, and #4 for the BIM implemented in the whole inversion domain have the largest values. By contrast, those for the BIM implemented in the imaging region obtained by U-Net have the smallest values among the three methods since the inversion domains restored by U-Net are close to the true scatterer shapes. Table I shows the model misfits of reconstructed permittivity and conductivity when iterations terminate. It can be seen that, among the three methods, the FWI based on U-Net has the smallest model misfit while that implemented in the whole inversion domain has the largest model misfit. These comparisons of data misfits and model misfits among different inversion methods quantitatively manifest the superiority of the prosed hybrid method for 3-D MWI. One interesting observation is that the model misfit values of conductivity are much larger than those of the permittivity. This is caused by the zero conductivity value of the free space background. The denominators in the model misfit calculation for conductivity are rather small (see [37, eq. (16)]), which causes large model misfit values. Another obvious superiority of the proposed hybrid method is its lowest computational cost due to the reduction of inversion domain. For example, in Test #4, there are totally 32 768, 1656, and 1435 voxels in the whole inversion domain, the inversion domain obtained by threshold cut, and by the U-Net refinement, respectively. This implies that the computational cost of the proposed hybrid 3-D method is also the lowest among the three methods. Numerical simulations show that the mean single-step iteration time of BIM performed in the whole inversion domain is 235 s, while that based on U-Net results is only 47 s in Test #4.

TABLE I
MODEL MISFITS (%) FOR BIM, LSM+TH+BIM, AND LSM+U-NET+BIM

Test \ Method		BIM	LSM+TH+BIM	LSM+U-Net+BIM
Test #1	ε	8.911	5.826	1.744
	σ	91.38	54.66	19.56
Test #2	ε	9.969	9.721	6.820
	σ	53.79	60.43	28.32
Test #3	ε	11.08	9.060	7.886
	σ	81.34	40.79	31.41
Test #4	ε	10.19	8.860	7.132
	σ	81.74	62.64	48.06

Remark: TH represents "threshold".

B. Case 2: Multiple Homogeneous Anisotropic Objects

In this case, we apply the proposed hybrid MWI method to the reconstruction of 3-D dielectric arbitrary anisotropic objects whose dielectric parameter tensors are symmetrical [34]. The simulated electric fields are contaminated by

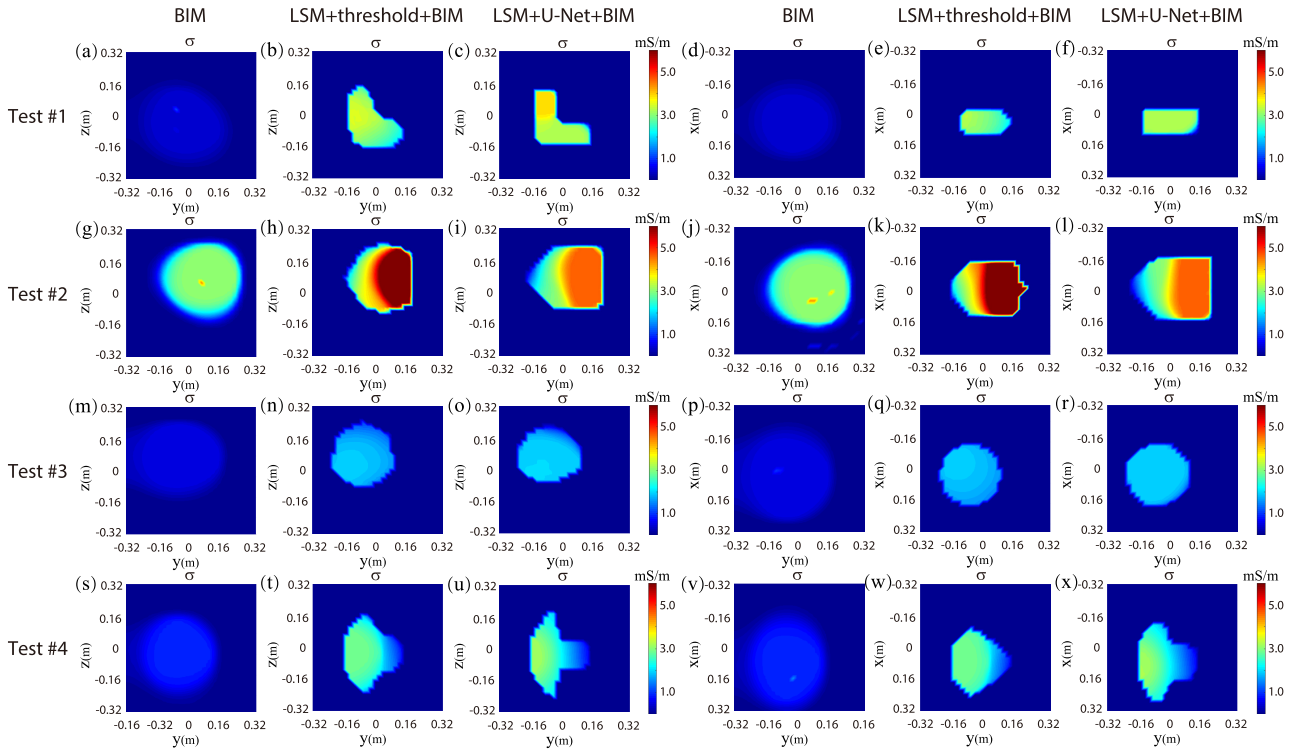

Fig. 5. FWI of conductivity values by BIM performed in the whole inversion domain, in the imaging region obtained by threshold cut, and in the imaging region refined by U-Net. Columns 1–3 show the 2-D yz slices of inversion results. Columns 4–6 show the 2-D xy slices of inversion results.

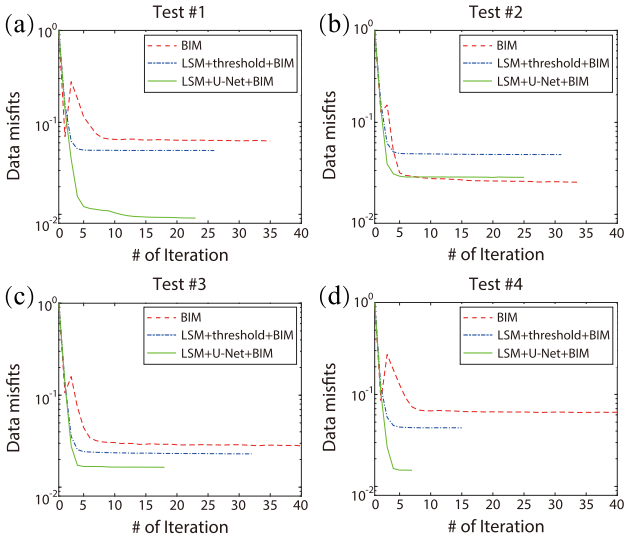

Fig. 6. BIM convergence curves in the four tests.

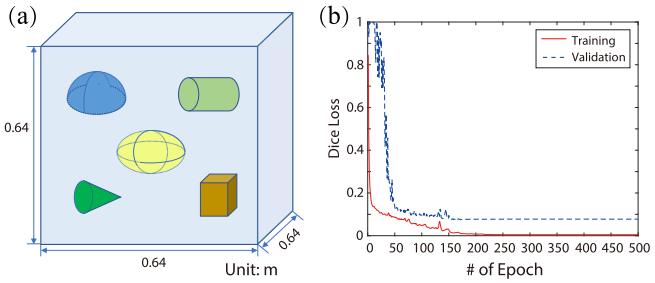

Fig. 7. (a) Anisotropic 3-D objects used for training the U-Net. (b) Convergence curves of training and validation.

20 dB white Gaussian noise which leads to approximately 10% errors. Here, the noise level is defined according to the

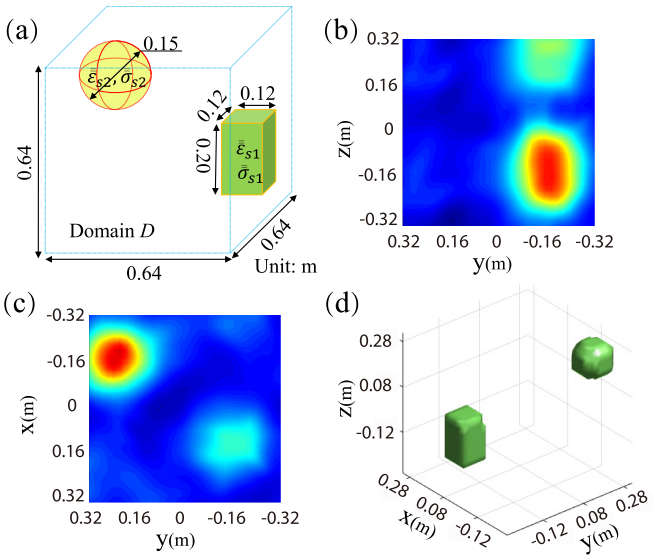

Fig. 8. (a) True shapes of the anisotropic cuboid and sphere. (b) Two-dimensional LSM image yz slice of the cuboid at $x = 0.1$ m. (c) Two-dimensional LSM image xy slice of the sphere at $z = 0.16$ m. (d) Refined shapes of two anisotropic objects by U-Net.

signal-to-noise ratio (SNR) of power, and the noise is added to the scattered field data instead of to the total field data. The Gaussian noise is generated by the MATLAB function wgn. The training dataset is constructed by randomly combing two basic shapes shown in Fig. 7(a) except the combination of a hemisphere and a cuboid which will be used in the testing. The diagonal elements of the relative permittivity tensor of the homogeneous object used in the training randomly change between 1.3 and 2.0 and the nondiagonal elements change

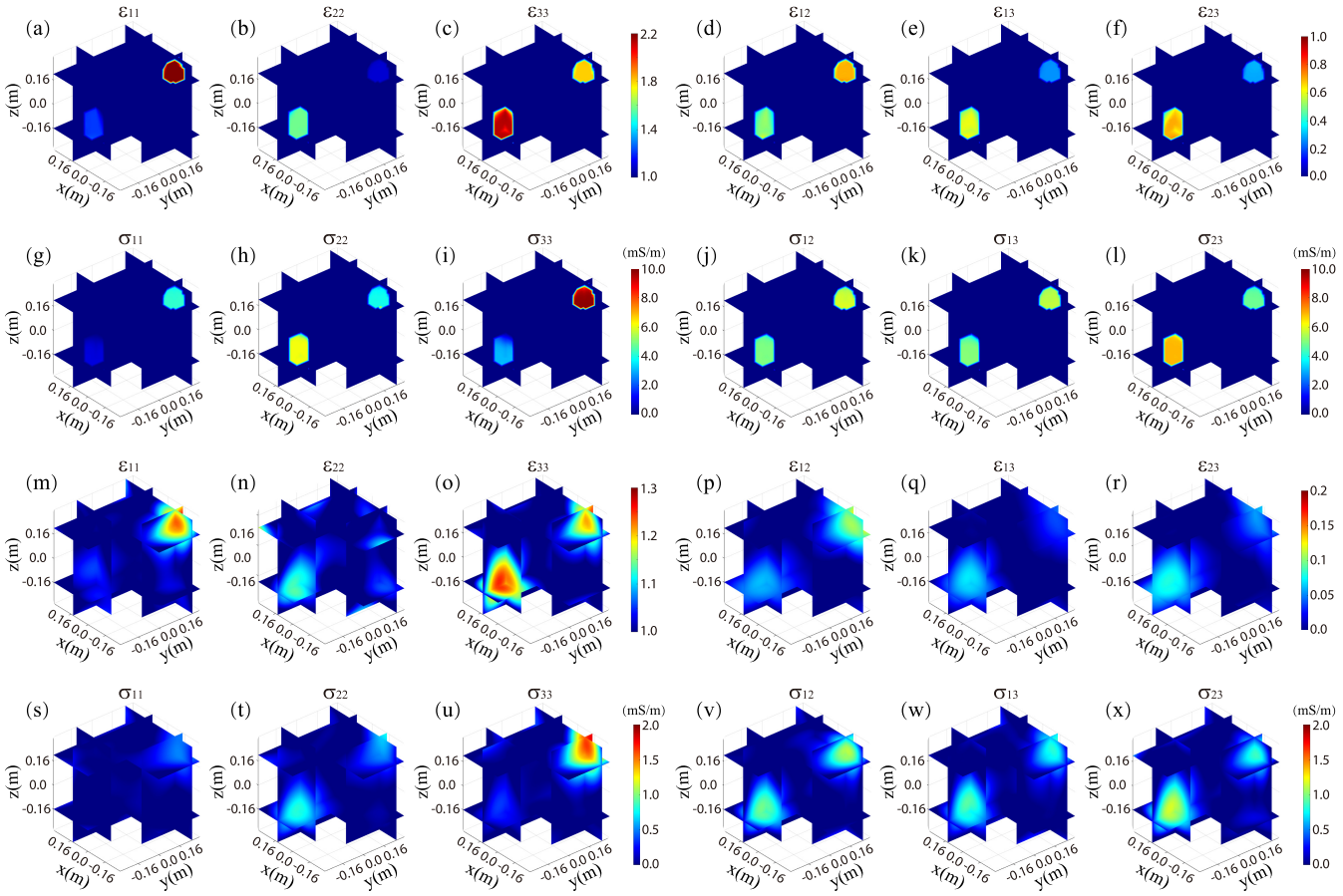

Fig. 9. Reconstructed anisotropic dielectric parameters of the cuboid and the sphere. (a)–(l) By BIM implemented in the inversion domain judged by U-Net. (m)–(x) By BIM implemented in the whole inversion domain.

TABLE II

RELATIVE PERMITTIVITY AND CONDUCTIVITY OF THE CUBOID AND SPHERE WITH DIELECTRIC ARBITRARY ANISOTROPY

	ε_{11}	ε_{12}	ε_{13}	ε_{22}	ε_{23}	ε_{33}	σ_{11}	σ_{12}	σ_{13}	σ_{22}	σ_{23}	σ_{33}
cuboid	1.2	0.5	0.6	1.6	0.7	2.1	1.0	5.0	5.0	6.0	7.0	3.0
sphere	2.2	0.7	0.3	1.1	0.3	1.8	5.0	6.0	6.0	4.0	5.0	10

Remark: the unit of σ is mS/m.

between 0.2 and 0.7. All the elements in the conductivity tensor range between 2 and 8 mS/m. Totally, 1100 3-D samples with dielectric arbitrary anisotropy are generated by LSM from scattered field data with 20 dB noise. Among them, 1000 samples are used for training and 100 ones are used for validation. Fig. 7(b) shows the convergence curves for both training and validation which have no obvious difference compared with the ones shown in Fig. 2(b).

In the online prediction, we apply LSM and the trained U-Net to the inversion of a sphere and a cuboid, as shown in Fig. 8(a). One should note that the combination of a sphere and a cuboid is not included in the training dataset. Such a choice is to test the generalization ability of the trained 3-D U-Net. The sizes of two objects are labeled in Fig. 8(a) and their dielectric parameter values are listed in Table II. Note we only consider the scatterers with symmetrical dielectric tensors, which is commonly seen in real-life applications, e.g., crystal inspection [38]. The values of some parameters actually fall out of the ranges of the parameter values of the training dataset, which is also used to test the generalization ability of the U-Net. In addition, the simulated scattered field data by these two objects are also contaminated by 20 dB noise. Figs. 8(b) and (c) respectively show the yz and xy slices of the same 3-D LSM image of the entire domain. One interesting observation is the existence of the phantom image of another object, which has not been found in Case 1. This may be caused by the mutual scattering among multiple objects. Fortunately, the phantom images are eliminated by the 3-D U-Net and its good output is displayed in Fig. 8(d).

We then perform the FWI by BIM in the restricted domain obtained via the U-Net refinement and the whole inversion domain, respectively. The 3-D results are shown in Fig. 9 and the model misfits for all reconstructed anisotropic dielectric parameters are listed in Table III. We can see that the proposed hybrid method also shows good performance for the inversion of anisotropic scatterers with 12 unknowns even when the scattered field data are contaminated by 20 dB noise. Not only the shapes of the cuboid and the sphere are precisely reconstructed, but also the values of their model parameters are accurately retrieved. This is manifested by the low model misfit values listed in Table III. By contrast, only two blurry objects show up in the 3-D imaging region if BIM is implemented in the whole inversion domain, as shown in the 3rd and

TABLE III
MODEL MISFITS (%) OF THE RECONSTRUCTED ANISOTROPIC DIELECTRIC PARAMETERS BY LSM+U-NET+BIM AND PURE BIM

	ϵ_{11}	ϵ_{22}	ϵ_{33}	ϵ_{12}	ϵ_{13}	ϵ_{23}	σ_{11}	σ_{22}	σ_{33}	σ_{12}	σ_{13}	σ_{23}
LSM+U-Net+BIM	1.146	0.710	1.956	11.24	12.55	11.89	22.57	17.87	14.98	13.36	14.80	13.60
BIM	9.533	6.408	11.65	91.88	92.70	92.56	95.45	92.16	90.69	88.67	90.69	89.79

4th rows of Fig. 9. Although the positions of the two objects are roughly correct, the shapes are severely distorted and the volume becomes very large. This leads to much smaller retrieved dielectric parameters compared to their true values and thus much larger model misfit values which are listed in Table III. Note for the reconstruction of anisotropic scatterers, the model misfit values of conductivity are also much less than those for the permittivity. The reason has been mentioned in Section III-A.

IV. CONCLUSION

This article is an extension of our previous work [26] and the counterpart of [27]. The threefold 3-D hybrid method is applied to quantitative MWI in which the scattered electric field data are recorded in the far-field zone and the receiver array wraps the imaging domain. A series of numerical experiments show that the proposed hybrid method can quantitatively and precisely image both the 3-D isotropic and anisotropic objects in a quite efficient way. In the first step, the 3-D LSM is employed to qualitatively reconstruct the approximate shapes and locations of the unknown objects. This step is very fast and is usually accomplished in a few seconds. In the second step, the shapes reconstructed by the LSM are improved by the 3-D CNN U-Net. One should note that this step is almost finished instantaneously by the online prediction although the offline training usually takes a long time. In the third step, although the FWI still needs iterations to obtain the dielectric parameter values, its computational cost is significantly lowered since it is only executed in a restricted region instead of in the whole domain. Finally, we want to emphasize that although the proposed hybrid method succeeds in the numerical examples, the issues such as the radiation pattern of transmitter antennas and recorded voltage of antenna output instead of the electric field quantity must be taken into account in practical engineering applications. In addition, the method also has some limitations. For example, the LSM may fail to generate reliable 3-D images of hollow objects, which will compromise the inversion ability of the following BIM solver. If the shapes of practical objects are far from those used in the training dataset, the U-Net may also fail to obtain reliable shapes.

APPENDIX

By referring to Fig. 1 and the derivation of electric fields in the far zone given in [39], we can obtain the far-field Green's function $\mathbf{f}_u^p(\mathbf{r}', \mathbf{r})$ as follows.

If the fictitious source point at $\mathbf{r}' \in D$ is $\hat{x}$ polarized, we have

$$\mathbf{f}_x^\theta(\mathbf{r}', \mathbf{r}) = A_1 \cdot A_2 \cdot \cos\theta\cos\phi \tag{A1a}$$

$$\mathbf{f}_x^\phi(\mathbf{r}', \mathbf{r}) = -A_1 \cdot A_2 \cdot \sin\phi. \tag{A1b}$$

If the fictitious source point at $\mathbf{r}' \in D$ is $\hat{y}$ polarized, we have

$$\mathbf{f}_y^\theta(\mathbf{r}', \mathbf{r}) = A_1 \cdot A_2 \cdot \cos\theta\sin\phi \tag{A2a}$$

$$\mathbf{f}_y^\phi(\mathbf{r}', \mathbf{r}) = A_1 \cdot A_2 \cdot \cos\phi. \tag{A2b}$$

If the fictitious source point at $\mathbf{r}' \in D$ is $\hat{z}$ polarized, we have

$$\mathbf{f}_z^\theta(\mathbf{r}', \mathbf{r}) = -A_1 \cdot A_2 \cdot \sin\theta \tag{A3a}$$

$$\mathbf{f}_z^\phi(\mathbf{r}', \mathbf{r}) = 0. \tag{A3b}$$

Note that the constants A_1 and A_2 in the above six formulas are defined as

$$A_1 = \frac{-j\omega\mu_0 \exp[-jk_0 r]}{4\pi r} \tag{A4a}$$

$$A_2 = \exp[jk_0(x'\sin\theta\cos\phi + y'\sin\theta\sin\phi + z'\cos\theta)] \tag{A4b}$$

where r is the length of $\mathbf{r} = x\hat{x} + y\hat{y} + z\hat{z}$ which denotes the position of the receiver and $\mathbf{r}' = x'\hat{x} + y'\hat{y} + z'\hat{z}$ denotes the position of the fictitious source point inside the imaging and inversion domain D.

REFERENCES

[1] G. Wang, X.-G. Xia, and V. C. Chen, "Radar imaging of moving targets in foliage using multifrequency multiaperture polarimetric SAR," *IEEE Trans. Geosci. Remote Sens.*, vol. 41, no. 8, pp. 1755–1764, Aug. 2003.

[2] P. Withington, H. Fluhler, and S. Nag, "Enhancing homeland security with advanced UWB sensors," *IEEE Microw. Mag.*, vol. 4, no. 3, pp. 51–58, Sep. 2003.

[3] T. P. Montoya and G. S. Smith, "Land mine detection using a ground-penetrating radar based on resistively loaded Vee dipoles," *IEEE Trans. Antennas Propag.*, vol. 47, no. 12, pp. 1795–1806, Dec. 1999.

[4] F. García-Rial, D. Montesano, I. Gómez, C. Callejero, F. Bazus, and J. Grajal, "Combining commercially available active and passive sensors into a millimeter-wave imager for concealed weapon detection," *IEEE Trans. Microw. Theory Techn.*, vol. 67, no. 3, pp. 1167–1183, Mar. 2019.

[5] D. O'Loughlin, M. O'Halloran, B. M. Moloney, M. Glavin, E. Jones, and M. A. Elahi, "Microwave breast imaging: Clinical advances and remaining challenges," *IEEE Trans. Biomed. Eng.*, vol. 65, no. 11, pp. 2580–2590, Nov. 2018.

[6] X. Feng and M. Sato, "Pre-stack migration applied to GPR for landmine detection," *Inverse Problems*, vol. 20, no. 6, pp. S99–S115, Dec. 2004.

[7] A. T. Mobashsher, A. M. Abbosh, and Y. Wang, "Microwave system to detect traumatic brain injuries using compact unidirectional antenna and wideband transceiver with verification on realistic head phantom," *IEEE Trans. Microw. Theory Techn.*, vol. 62, no. 9, pp. 1826–1836, Sep. 2014.

[8] R. Chandra, H. Zhou, I. Balasingham, and R. M. Narayanan, "On the opportunities and challenges in microwave medical sensing and imaging," *IEEE Trans. Biomed. Eng.*, vol. 62, no. 7, pp. 1667–1681, Jul. 2015.

[9] M. F. Imani *et al.*, "Review of metasurface antennas for computational microwave imaging," *IEEE Trans. Antennas Propag.*, vol. 68, no. 3, pp. 1860–1875, Mar. 2020.

[10] Y. Jia, G. Cui, L. Kong, and X. Yang, "Multichannel and multiview imaging approach to building layout determination of through-wall radar," *IEEE Geosci. Remote Sens. Lett.*, vol. 11, no. 5, pp. 970–974, May 2014.

[11] L. Ding, X. L. Deán-Ben, and D. Razansky, "Real-time model-based inversion in cross-sectional optoacoustic tomography," *IEEE Trans. Med. Imag.*, vol. 35, no. 8, pp. 1883–1891, Aug. 2016.

[12] T. M. Habashy, R. W. Groom, and B. R. Spies, "Beyond the Born and Rytov approximations: A nonlinear approach to electromagnetic scattering," *J. Geophys. Res., Solid Earth*, vol. 98, no. B2, pp. 1759–1775, 1993.
[13] H. Liu, Z. Long, F. Han, G. Fang, and Q. H. Liu, "Frequency-domain reverse-time migration of ground penetrating radar based on layered medium Green's functions," *IEEE J. Sel. Topics Appl. Earth Observ. Remote Sens.*, vol. 11, no. 8, pp. 2957–2965, Aug. 2018.
[14] I. Catapano, L. Crocco, and T. Isernia, "On simple methods for shape reconstruction of unknown scatterers," *IEEE Trans. Antennas Propag.*, vol. 55, no. 5, pp. 1431–1436, May 2007.
[15] K. Ito, B. Jin, and J. Zou, "A direct sampling method to an inverse medium scattering problem," *Inverse Problems*, vol. 28, no. 2, Jan. 2012, Art. no. 025003.
[16] M. T. Bevacqua, T. Isernia, R. Palmeri, M. N. Akıncı, and L. Crocco, "Physical insight unveils new imaging capabilities of orthogonality sampling method," *IEEE Trans. Antennas Propag.*, vol. 68, no. 5, pp. 4014–4021, May 2020.
[17] M. R. Eskandari, M. Dehmollaian, and R. Safian, "Experimental investigation of factorization method as a qualitative approach for near-field microwave imaging," *IEEE Antennas Wireless Propag. Lett.*, vol. 13, pp. 289–292, 2014.
[18] W. C. Chew and Y. M. Wang, "An iterative solution of the two-dimensional electromagnetic inverse scattering problem," *Int. J. Imag. Syst. Technol.*, vol. 1, pp. 100–108, Jan. 1989.
[19] P. M. Van Den Berg and R. E. Kleinman, "A contrast source inversion method," *Inverse Probl.*, vol. 13, no. 6, pp. 1607–1620, Jul. 1997.
[20] X. Chen, "Subspace-based optimization method for solving inverse-scattering problems," *IEEE Trans. Geosci. Remote Sens.*, vol. 48, no. 1, pp. 42–49, Jan. 2010.
[21] D. W. Winters, J. D. Shea, P. Kosmas, B. D. Van Veen, and S. C. Hagness, "Three-dimensional microwave breast imaging: Dispersive dielectric properties estimation using patient-specific basis functions," *IEEE Trans. Med. Imag.*, vol. 28, no. 7, pp. 969–981, Mar. 2009.
[22] N. Zaiping, Y. Feng, Z. Yanwen, and Z. Yerong, "Variational Born iteration method and its applications to hybrid inversion," *IEEE Trans. Geosci. Remote Sens.*, vol. 38, no. 4, pp. 1709–1715, Jul. 2000.
[23] K. Xu, Y. Zhong, R. Song, X. Chen, and L. Ran, "Multiplicative-regularized FFT twofold subspace-based optimization method for inverse scattering problems," *IEEE Trans. Geosci. Remote Sens.*, vol. 53, no. 2, pp. 841–850, Feb. 2015.
[24] X. Ye and X. Chen, "Subspace-based distorted-Born iterative method for solving inverse scattering problems," *IEEE Trans. Antennas Propag.*, vol. 65, no. 12, pp. 7224–7232, Dec. 2017.
[25] J. Li, J. Zhuo, Z. Guan, F. Han, and Q. H. Liu, "3-D electromagnetic scattering and inverse scattering by magnetodielectric objects with arbitrary anisotropy in layered uniaxial media," *IEEE Trans. Antennas Propag.*, vol. 68, no. 2, pp. 1009–1022, Feb. 2020.
[26] Y. Chen, L.-Y. Xiao, J. Zhuo, F. Han, and Q. Huo Liu, "Quantitative electromagnetic inversion of irregular scatterers based on a threefold hybrid method," *IEEE Trans. Antennas Propag.*, vol. 69, no. 12, pp. 8664–8674, Dec. 2021.
[27] M. Zhong, Y. Chen, J. Li, and F. Han, "Reconstruction of subsurface objects by LSM and FWI from limited-aperture electromagnetic data," *IEEE Trans. Geosci. Remote Sens.*, vol. 60, 2022, Art. no. 2003011.
[28] G. Chen, P. Shah, J. Stang, and M. Moghaddam, "Learning-assisted multimodality dielectric imaging," *IEEE Trans. Antennas Propag.*, vol. 68, no. 3, pp. 2356–2369, Mar. 2020.
[29] P. Mojabi, M. Hughson, V. Khoshdel, I. Jeffrey, and J. LoVetri, "CNN for compressibility to permittivity mapping for combined ultrasound-microwave breast imaging," *IEEE J. Multiscale Multiphys. Comput. Techn.*, vol. 6, pp. 62–72, 2021.
[30] V. Khoshdel, M. Asefi, A. Ashraf, and J. LoVetri, "A multi-branch deep convolutional fusion architecture for 3D microwave inverse scattering: Stored grain application," *Neural Comput. Appl.*, vol. 33, no. 20, pp. 13467–13479, Oct. 2021.
[31] D. Colton, H. Haddar, and M. Piana, "The linear sampling method in inverse electromagnetic scattering theory," *Inverse Problems*, vol. 19, no. 6, pp. S105–S137, Nov. 2003.
[32] G. L. Wang, T. Barber, P. Wu, D. Allen, and A. Abubakar, "Fast inversion of triaxial induction data in dipping crossbedded formations," *Geophysics*, vol. 82, no. 2, pp. D31–D45, Mar. 2017.
[33] W. C. Chew, *Waves Fields Inhomogeneous Media*. New York, NY, USA: IEEE, 1995, ch. 7.
[34] J. Fei, Y. Chen, M. Zhong, and F. Han, "Fast 3-D electromagnetic full-wave inversion of dielectric anisotropic objects based on ResU-Net enhanced by variational Born iterative method," *IEEE Trans. Antennas Propag.*, vol. 70, no. 8, pp. 6229–6239, Aug. 2022.
[35] F. Li, Q. H. Liu, and L.-P. Song, "Three-dimensional reconstruction of objects buried in layered media using Born and distorted Born iterative methods," *IEEE Geosci. Remote Sens. Lett.*, vol. 1, no. 2, pp. 107–111, Apr. 2004.
[36] B. Wohlberg and P. Rodriguez, "An iteratively reweighted norm algorithm for minimization of total variation functionals," *IEEE Signal Process. Lett.*, vol. 14, no. 12, pp. 948–951, Dec. 2007.
[37] T. Lan, N. Liu, F. Han, and Q. H. Liu, "Joint petrophysical and structural inversion of electromagnetic and seismic data based on volume integral equation method," *IEEE Trans. Geosci. Remote Sens.*, vol. 57, no. 4, pp. 2075–2086, Apr. 2019.
[38] P. P. Natali, L. Montalto, D. Rinaldi, F. Davi, N. Paone, and L. Scalise, "Noninvasive inspection of anisotropic crystals: Innovative photoelasticity-based methods," *IEEE Trans. Nucl. Sci.*, vol. 65, no. 8, pp. 2203–2207, Aug. 2018.
[39] C. A. Balanis, *Advanced Engineering Electromagnetics*. New York, NY, USA: Wiley, 2012, ch. 6.

Feng Han (Senior Member, IEEE) received the B.S. degree in electronic science from Beijing Normal University, Beijing, China, in 2003, the M.S. degree in geophysics from Peking University, Beijing, in 2006, and the Ph.D. degree in electrical engineering from Duke University, Durham, NC, USA, in 2011.

Since July 2015, he has been with Xiamen University, Xiamen, China, where he is currently an Associate Professor with the Institute of Electromagnetics and Acoustics. He has published over 50 articles in refereed journals. His research interests include electromagnetic scattering and inverse scattering in complex media, multiparametric and multidimensional hybrid electromagnetic full-wave inversion, fast electromagnetic full-wave inversion based on machine learning, configuration of the antenna array for electromagnetic inverse problems, and geophysical electromagnetic exploration and inversion.

Miao Zhong received the B.E. degree in communication engineering from Nanchang Hangkong University, Nanchang, China, in 2020. She is currently pursuing the master's degree with Xiamen University, Xiamen, China.

Her research interests include electromagnetic inverse scattering and full-wave inversion.

Junjie Fei received the B.E. degree in communication engineering from Chongqing University, Chongqing, China, in 2020. He is currently pursuing the master's degree with Xiamen University, Xiamen, China.

His research interests include artificial intelligence, machine learning, and applying these techniques to electromagnetic inverse scattering and imaging problems.